Scaling and the approach to scaling at large transverse momentum

R. Michael Barnett and D. Silverman*
Department of Physics, University of California, Irvine, Irvine, California 92664

(Received 14 January 1974)

Large transverse-momentum scaling as $E d\sigma/d^3p = p_\perp^{-8} f(x_\perp, x_\parallel)$ is first discussed in terms of models of parton-parton scattering. We review explicitly the equivalence of this approach to the multiperipheral and field-theory approaches, and we find the parton distribution function that fits the recent CERN ISR and NAL data. Then the deviations from scaling at nonasymptotic energies due to internal and external masses are examined by an exact numerical calculation of the general peripheral structure for the single-particle spectrum, which includes the parton models. This provides good fits to the single-particle spectra at all $p_\perp$ and explains the observed deviations from scaling at small $p_\perp$. The rise of the central plateau, secondary trajectories, and particle ratios at large $p_\perp$ are also discussed.

I. INTRODUCTION

A general peripheral formulation for the single-particle spectra has been successful in describing features of particle production at small transverse momentum $p_\perp$.[1] We have recently shown[2] that the power-law $p_\perp^{-8}$ behavior at fixed $p_\perp$ at asymptotic energy results from power-law internal damping in momentum transfers in a general peripheral structure, Fig. 1, and that the large-$p_\perp$ behavior joins smoothly onto the small-$p_\perp$ central plateau. In addition Amati, Caneschi, and Testa[3] (ACT) have shown that large-transverse-momentum scaling results from the ABFST[4] (Amati, Bertocchi, Fubini, Stanghellini, and Tonin) multiperipheral models; that is, in the limit $s \to \infty$ with $x_\perp = 2p_\perp/s^{1/2}$ and $x_\parallel = 2p_\parallel/s^{1/2}$ fixed, the single-particle spectrum behaves as

$$E\frac{d\sigma}{d^3p} = \frac{1}{p_\perp{}^n} f(x_\perp, x_\parallel) \ . \tag{1.1}$$

This large-transverse-momentum or fixed-$x_\perp$ scaling had previously been found from parton-parton scattering models (Fig. 2), including quark-quark scattering with vector exchange ($n=4$) by Berman, Bjorken, and Kogut[5] (BBK), from quark interchange ($n=8$) by Blankenbecler, Brodsky, and Gunion[6] (BBG), and from vector exchange to pions with form factors ($n=8$) by Bander, Barnett, and Silverman[7] (BBS).

Landshoff and Polkinghorne[8,9] have shown that the covariant field-theory method of calculation is equivalent to the infinite-momentum method results of BBG and to the multiperipheral ABFST diagram of Fig. 1 as used by ACT[3] and ourselves.[2] A comparison of the Landshoff-Polkinghorne result, Eq. (3.4) of Ref. 8, and Eq. (3.54) of BBK[5] shows that in general all of these approaches agree with the BBK parton-parton scattering method. The assumptions of the quantum numbers of the partons and their interactions with hadrons are then the main differences of the above papers, other than the methods used to calculate diagrams of the same structure.

In Sec. II we explicitly use the BBK method of parton-parton scattering, Fig. 2, applied for simplicity to spinless partons, and show that it yields precisely the same scaling form as results from the ABFST multiperipheral approach[3] or the field-theory approach[6,8] and may be considered a simple derivation of the result. The spinless-parton model leads naturally to the power-law result ($n=8$)

$$E\frac{d\sigma}{d^3p} = \frac{1}{p_\perp{}^8} f(x_\perp, x_\parallel) \tag{1.2}$$

that is in agreement with recent ISR data.[10] In parton models with other spins present, form factors are or can be included to give the observed $p_\perp{}^{-8}$ behavior. The difference is then only in the angular dependence of the parton-parton scattering cross section, which is rather washed out by the integration to obtain the inclusive spectra.[11] BBG[6] have also noted that the simplification of neglecting spin does not alter general dynamical features.

In this rather general formulation we then find the parton momentum-distribution function that fits the observed $x_\perp$ dependence at $x_\parallel = 0$. We also find the $\cos\theta = x_\parallel/(x_\parallel{}^2 + x_\perp{}^2)^{1/2}$ angular dependence of the inclusive cross section which can be used to compare various models. In Appendix A we show explicitly for this simplified spinless case the connection between the parton-parton approach (Fig. 2) and the general peripheral approach (Fig. 1).

In Sec. III we examine the deviations from fixed $x_\perp$ scaling that occur at finite energy due to internal and external masses. We do this by an exact numerical calculation of the general peripheral structure for the single-particle spectrum, Fig. 1. We emphasize that these results do not depend on any particular choice of parton model, but apply

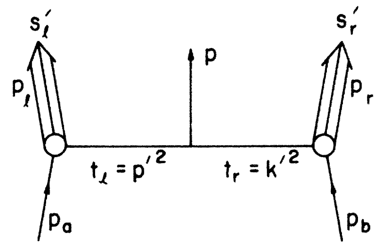

FIG. 1. Peripheral production diagram for the single-particle spectrum.

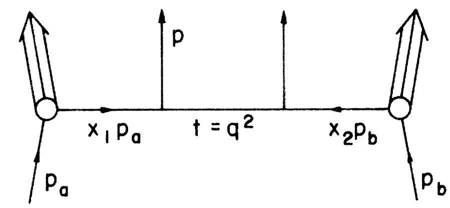

FIG. 2. Parton of momentum fraction x_1 elastically scattering from parton of fraction x_2 at large t with cross section $d\sigma/dt$.

to any model with internal damping that yields $p_\perp^{-8}$ scaling, Eq. (1.2), as considered necessary to fit the present data.[10,12] The finite-energy effects occur at low $p_\perp$, where internal exchanged masses affect the low-momentum-transfer region.

We use Bjorken scaling functions for the absorptive parts A_l and A_r for incoming momentum transfers t_l, t_r and for the left and right moving missing masses s_l' and s_r' in Fig. 1. Bjorken scaling is known to result from a multiperipheral structure[13,14] or from parton models.[15] We find the Bjorken-scaling functions that fit the fixed-$x_\perp$ scaling spectra. Then by introducing an internal mass parameter we can fit the data over the entire $p_\perp$ range at finite energies. The deviations from scaling at small $x_\perp$ at NAL and CERN ISR energies are also well fitted by the finite-energy calculation.

The dependence on the center-of-mass angle is calculated for a future experimental test and comparison with other models. The effect of secondary Regge trajectories was investigated and found not to change significantly the shape of the fixed-$x_\perp$ scaling spectra.

With these fits we found that the height of the central plateau, $d\sigma/dy$, in the equivalent of the double-Pomeron-exchange Mueller diagram, showed a rising approach to the asymptotic constant value. This is the same conclusion as obtained by Caneschi,[16] and is important in considering the experimentally observed rise.

The K^+/π^+ ratio was also calculated at finite energy and was found to differ little from the infinite-energy, finite-$p_\perp$ results reported previously.[17]

In Sec. II, the parton-parton scattering approach is presented. The numerical calculation of the approach to scaling at finite energy and its experimental effects are presented in Sec. III. Appendix A contains a calculation of the relation between the approaches of Secs. II and III, thereby allowing a quantitative justification of the approximations used in proving scaling. Appendix B contains kinematical details of the general peripheral approach of Sec. III.

II. SCALING AT FIXED $x_\perp$

In this section we show that the fixed-$x_\perp$ scaling result for multiperipheral models (ACT) (see Fig. 1) can be derived using the parton-scattering methods of Berman, Bjorken, and Kogut.[5,18] For the simplified case of spinless partons the resulting scaling law is

$$E\frac{d\sigma}{d^3p} = \frac{1}{p_\perp^{8}} f(x_\perp, x_\parallel) . \tag{2.1}$$

Since this scaling is consistent with the data, we also find the parton distribution function $P(x)$ and the resultant $f(x_\perp, x_\parallel)$ that fit the data.

An incoming particle of momentum p_a is viewed as a collection of partons with fractional momentum $x_1 p_a$ distributed by the probability $P(x_1)$. A parton from particle a and another from b then suffer a hard elastic collision by exchange of another particle or a constituent interchange with a differential cross section $(d\sigma/dt)(\hat{s}, t)$ at large momentum transfer $t = q^2 = O(s)$, Fig. 2. One of the scattered particles is then observed at momentum p. For $s \gg (\text{mass})^2$, we may write the parton momenta k_a, k_b as

$$\begin{aligned} k_a &= x_1 p_a = x_1 \tfrac{1}{2} s^{1/2}(1, \hat{z}) , \\ k_b &= x_2 p_b = x_2 \tfrac{1}{2} s^{1/2}(1, -\hat{z}) . \end{aligned} \tag{2.2}$$

The observed momentum in terms of scaling variables is

$$p = \tfrac{1}{2} s^{1/2}\big((x_\perp^2 + x_\parallel^2)^{1/2}, x_\perp, x_\parallel\big) , \tag{2.3}$$

where $x_\perp = 2p_\perp/s^{1/2}$ denotes a two-dimensional transverse vector. Also

$$q = -\tfrac{1}{2} s^{1/2}\big((x_\perp^2 + x_\parallel^2)^{1/2} - x_1, x_\perp, x_\parallel - x_1\big) . \tag{2.4}$$

The cross section for the graph[5] in Fig. 2 is the probability for partons at fractions x_1 and x_2 scattering by the elastic cross section $d\sigma/dt$:

$$d\sigma = P(x_1)dx_1 P(x_2)dx_2 \frac{d\sigma}{dt}\, dt . \tag{2.5}$$

The elastic scattering takes place with an invariant energy

$$\hat{s} = (k_a + k_b)^2 = s x_1 x_2 \tag{2.6}$$

and a momentum transfer

$$t = q^2 \approx -2p \cdot k_a = -s x_1 x_- , \tag{2.7}$$

where we define the convenient scaled "light cone" variables

$$\begin{aligned} x_\pm &\equiv \tfrac{1}{2}[(x_\perp^2 + x_\parallel^2)^{1/2} \pm x_\parallel] , \\ x_+ x_- &= \tfrac{1}{4} x_\perp^2 . \end{aligned} \tag{2.8}$$

For a relatively free parton, k_b^2 will be small, and $2k_b \cdot q \approx -q^2$ yields the restriction

$$x_2 = \frac{x_1 x_-}{x_1 - x_+} . \tag{2.9}$$

The relation of the phase space in Eq. (2.5) to that of the observed particle in the single-particle spectrum is then

$$dt\, dx_2 \frac{d\phi}{2\pi} = \frac{1}{\pi} \frac{x_1^2 x_-}{(x_+ - x_1)^2} \frac{d^3p}{E} . \tag{2.10}$$

The elastic cross section for the scattering of spinless partons by a spinless exchange in the limit $s, |t| \gg (\text{mass})^2$ is

$$\frac{d\sigma}{dt} = \frac{\pi \alpha^2 m^4}{\hat{s}^2 t^2} , \tag{2.11}$$

where $\alpha m^2 = (gm)^2/4\pi$ and (gm) is the vertex coupling strength with dimensions of mass. Models with partons or exchanges having spin give $d\sigma/dt \propto \hat{s}^{-2} h(t/\hat{s})$, to which one must add a form factor squared $F^2(t) \propto m^4/t^2$ to agree with the $p_\perp^{-8}$ scaling. These models then only differ by their angular dependence $h(t/\hat{s})$.

We note from Eqs. (2.7), (2.9), and (2.10) that x_1, x_2 occur in the ratios

$$y = \frac{x_+}{x_1} , \quad 1 - y = \frac{x_-}{x_2} . \tag{2.12}$$

$P(x)$ will have a pionization distribution $P(x) \sim 1/x$ as $x \to 0$. Therefore we can define

$$P(x) = F(x)/x . \tag{2.13}$$

Then using Eqs. (2.5) and (2.10)–(2.13) we have the single-particle spectrum as an integral over x_1 or y:

$$E \frac{d\sigma}{d^3p} = \frac{\alpha^2 m^4}{p_\perp^8} \int_{x_+}^{1-x_-} dy\, F\left(\frac{x_+}{y}\right) F\left(\frac{x_-}{1-y}\right) y^3 (1-y) + (x_+ \to x_-) \tag{2.14}$$

The crossed graph where the other particle is detected is included in Eq. (2.14) by interchanging x_+ and x_-. This result shows explicitly the $p_\perp^{-8}$ behavior resulting from the dimensioned coupling constant for spinless vertices or from form factors. The scaling behavior of $p_\perp^8(E d\sigma/d^3p)$ [Eq. (2.1)] in terms of x_+, x_- or $x_\perp$, $x_\parallel$ is also explicit. The form of Eq. (2.14) agrees with that of Landshoff and Polkinghorne[8] derived from Fig. 2 by field-theoretic methods.

We now show the relation of this approach to the ABFST multiperipheral model.[3,4] By changing the integration variable to

$$\omega = (1-y)/x_- = 1/x_2 , \tag{2.15}$$

with

$$\chi(\omega) \equiv F(1/\omega) , \tag{2.16}$$

we obtain

$$E \frac{d\sigma}{d^3p} = \frac{\alpha^2 m^4 x_-^2}{p_\perp^8} \int_1^{(1-x_+)/x_-} d\omega\, \chi\left(\frac{1 - x_- \omega}{x_+}\right) \times \chi(\omega)(1 - x_- \omega)^3 \omega . \tag{2.17}$$

This agrees precisely with the result of ACT[3] if applied to spinless particles. ACT started from the equation for the single-particle spectrum in the ABFST multiperipheral model[4] with power-law damping in momentum transfer and evaluated it in the fixed-$x_\perp$, $x_\parallel$ scaling limit. (The evaluation of the fixed-$x_\perp$, $x_\parallel$ scaling limit for exponential damping was previously performed by Silverman and Tan.[19]). Thus, the parton-scattering approach of BBK[5] is equivalent to the ABFST multiperipheral approach.

While the $p_\perp^{-8}$ behavior follows from the above considerations, the actual distribution function $P(x)$ for the partons has to be phenomenologically fitted to the scaling distribution $f(x_\perp, x_\parallel)$. The presently available data can be fitted with the parton distribution

$$P(x) = (1-x)^4/x . \tag{2.18}$$

The comparison with the $x_\parallel = 0$ CERN ISR scaling data[10] over a range of energies is shown in Fig. 3. In Fig. 4 we show the comparison with the NAL data[12] out to larger $x_\perp$. The drop of the data and nonscaling for small $x_\perp$ is due to the nonasymptotic energies as explained in Sec. III. Finally, in Fig. 5 the data[20] at 60° c.m. at the CERN ISR are plotted; the calculated result with this approach is very close to that of Sec. III, shown in Fig. 5.

The angular dependence of the cross section is also of great experimental and theoretical interest. Theoretically, since the scattered partons in Fig. 2 are not always alike, the distribution functions $P_1(x_1)$ and $P_2(x_2)$ are expected to be different. These can only be isolated by separately varying x_+ and x_- in Eq. (2.14). Experimentally, the data is limited by the event rate at large $p_\perp$. However, one can also stay at fixed radius $r = (x_\perp^2 + x_\parallel^2)^{1/2}$ in the $x_\perp$, $x_\parallel$ phase space and vary the angle z

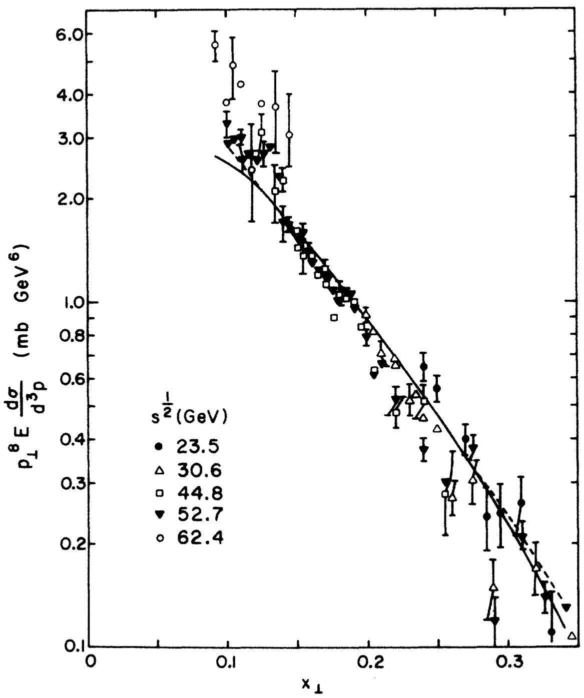

FIG. 3. The single-particle spectrum times $p_\perp{}^8$ at $x_\parallel = 0$ for $pp \to \pi + X$ as a function of $x_\perp = 2p_\perp/s^{1/2}$. The data are from Ref. 10 and sample error bars are shown. The dashed line is the fit of Sec. II and the solid line is that of Sec. III with $s^{1/2} = 52.7$ GeV.

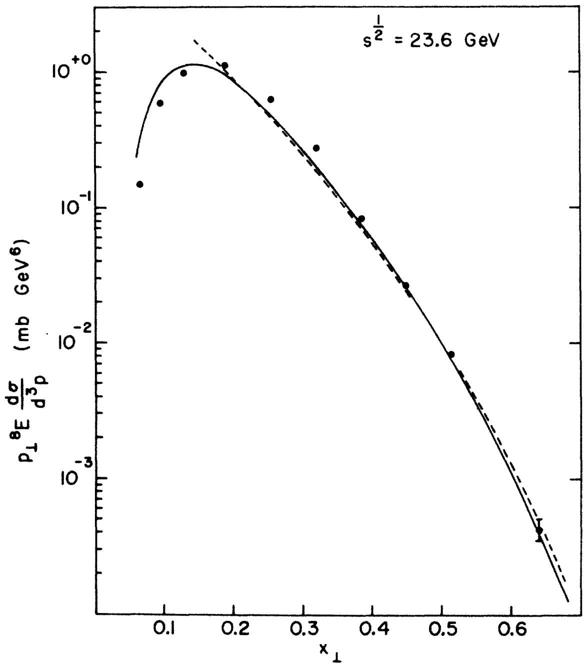

FIG. 4. The single-particle spectrum times $p_\perp{}^8$ at $x_\parallel = 0$ for $pp \to \pi + X$ as a function of $x_\perp$. The data are from Ref. 12 with the normalization decreased by a factor of two for consistency with the data of Ref. 10 at the same energy. The dashed line is the fit of Sec. II and the solid line is that of Sec. III with $s^{1/2} = 23.6$ GeV and $a^2 = 0.39$ GeV^2.

$= \cos\theta$. The dependence on z, as illustrated in Sec. III is much slower than that of the BBS model and may be used to distinguish various models even at the present event rate.[11]

III. APPROACH TO SCALING

A. Formulation

We now examine the effects at finite energy which modify scaling due to the presence of thresholds and internal masses in form factors and propagators. In order to calculate at finite energy and for both small and large transverse momentum, we use the general peripheral approach to the single-particle spectrum, Fig. 1. This single-particle spectrum has been formulated in Ref. 19 and can be expressed as

$$E\frac{d\sigma}{d^3p} = \frac{1}{s}\int d^4p' \int d^4k' \delta^4(p'+k'+p) \times \beta_l{}^2(t_l)\beta_r{}^2(t_r) \times A_l(s_l', t_l)A_r(s_r', t_r)\,, \quad (3.1)$$

where β_l and β_r contain the propagators of the exchanges and the central-vertex form factors, when necessary, and A_l and A_r are the off-shell absorptive parts from the inclusively summed par-

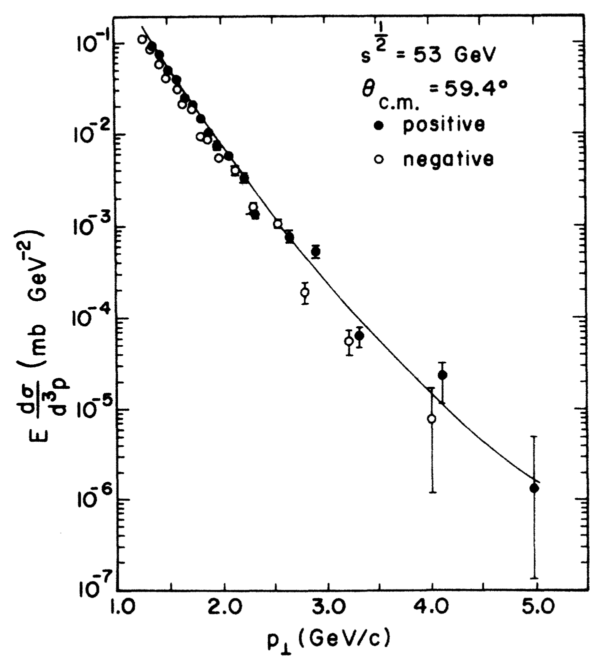

FIG. 5. The single-particle spectrum at $\theta_{c.m.} = 59.4°$ for $pp \to \pi + X$. The line is the result from Sec. III for $s^{1/2} = 53$ GeV. The data are from Ref. 20.

ticles.

To illustrate general effects of the approach to scaling, we work with models with sufficient damping in t_l, t_r to yield a $p_\perp^{-8}$ scaling law, Eq. (1.2). It is apparent that for power-law damping, when $p_\perp^2$ is large, the largest contribution results when one but not both of t_l and $t_r \approx O(p_\perp^2)$, as is the case in parton-parton scattering (see Sec. II).

The proper powers for $p_\perp^{-8}$ result naturally from all spin-zero partons (ϕ^3 model), while for most models which involve spin-$\frac{1}{2}$–quark exchange,[8,9] constituent interchange,[6] or vector gluons[5,7] the additional needed powers of t_l, t_r are put in as form factors. The difference in calculating these models, when adapted to $p_\perp^{-8}$ scaling, will only be in the angular dependence of the parton-parton cross section for the spins involved, which would show up in Eq. (3.1) as a modifying polynomial in $t/\hat{s}$, where

$$\frac{t}{s} = -\frac{s_r'/s + \frac{1}{4}x_\perp^2}{s_r'/s + x_+} .$$

For illustrating the effects at finite energy we can neglect these differences in Eq. (3.1).

Defining

$$\omega_l = \frac{s_l'}{a^2 - t_l} + 1 , \tag{3.2}$$

with a mass parameter a, we assume the off-shell absorptive parts obey Bjorken scaling,

$$A_l(s_l', t_l) = \frac{1}{a^2 - t_l}\, \omega_l\, \chi(\omega_l) , \tag{3.3}$$

and are Pomeron-dominated for fixed t_l with $s_l' \to \infty$, i.e.,

$$\chi(\omega_l) \xrightarrow[\omega_l \to \infty]{} 1 . \tag{3.4}$$

We take the propagators as

$$\beta_l(t_l) = \frac{1}{a^2 - t_l} , \tag{3.5}$$

and the symmetrical forms are assumed for ω_r, A_r, β_r also. While the breakup, Eq. (3.3) and (3.5), is natural to a ϕ^3 theory, the product $\beta_l^2 A_l$ will be the same for any $p_\perp^{-8}$ scaling theory as discussed above.

The resultant integrations from Eq. (3.1) are[19]

$$E\frac{d\sigma}{d^3p} = \frac{1}{2\Delta^{1/2}(s, m_1^2, m_2^2)} \int_{s_1}^{s_2} ds_r' \int_{s_3}^{s_4} ds_l' \int_{t_1}^{t_2} dt_r \int_{t_3}^{t_4} dt_l\, \frac{\theta(-\Delta_4)}{(-\Delta_4)^{1/2}}\, \frac{\omega_l \chi(\omega_l)}{(a^2 - t_l)^3}\, \frac{\omega_r \chi(\omega_r)}{(a^2 - t_r)^3} , \tag{3.6}$$

where the Jacobian and the limits are defined in Appendix B. This general form (but with arbitrary power damping) was approximated at $s \to \infty$ by ACT[3] and shown to lead to fixed-$x_\perp$ scaling, giving the result Eq. (2.17) for the case of $p_\perp^{-8}$ scaling.

B. General results

We find that the Bjorken-scaling form for parton distributions in the proton (with $x = 1/\omega$),

$$\omega\chi(\omega) = \omega\,\frac{(\omega - 1)^3}{\omega^3} = \frac{(1-x)^3}{x} , \tag{3.7}$$

with the same threshold behavior as electroproduction, gives a good fit to the $x_\perp$ distribution.

Doing the integrations in Eq. (3.6) numerically with $a^2 = 0.39$ GeV^2, the above form in Eq. (3.6) gives a good fit (Fig. 6; see Refs. 21 and 22) to the entire $p_\perp$ range of CERN ISR data, 0.2 GeV/c $< p_\perp <$ 9.0 GeV/c, at $x_\parallel = 0$ and $s^{1/2} = 52.7$ GeV.

The data at other CERN ISR energies can be examined in a scaling plot of $p_\perp^8 E d\sigma/d^3p$ versus $x_\perp$ (Fig. 3), and the fit with the above form [Eq. (3.7)] and value of a^2 is shown. Taking another view of these data, we fitted the rise of the spectra at fixed $p_\perp$ with increasing s.

At small $p_\perp$, the effects of exchanged mass a^2 and external masses become significant. Since these occur for a given $p_\perp$ range independent of energy, the region of small $x_\perp$ where they are significant decreases with increasing energy. These deviations from a scaling curve do not appear in Fig. 3 since all data were taken for $p_\perp > 1.5$ GeV/c. In Fig. 4 we show the NAL data[12] and the experimental deviation from the scaling curve for $x_\perp < 0.2$ ($s^{1/2} = 23.6$ GeV), along with our calculations.

We can determine the value of $x_\perp$ at which the data for $p_\perp^8 E d\sigma/d^3p$ turn over and deviate from scaling by noting that a good parametrization of the data for $x_\perp < 0.3$ (see Fig. 6 for $s^{1/2} = 52.7$ GeV) is

$$E\frac{d\sigma}{d^3p} = \frac{12.7 e^{(-13x_\perp)}}{(p_\perp^2 + 0.57)^4}\ \text{mb/GeV}^2 , \tag{3.8}$$

$$p_\perp^8 E\frac{d\sigma}{d^3p} = 12.7 e^{(-13x_\perp)} \left(1 + \frac{4(0.57)}{s x_\perp^2}\right)^{-4} \text{mb GeV}^6 . \tag{3.9}$$

The peak of this curve, Eq. (3.9), is given by

$$13 + \frac{52(0.57)}{s x_\perp^2} = \frac{32(0.57)}{s x_\perp^3} . \tag{3.10}$$

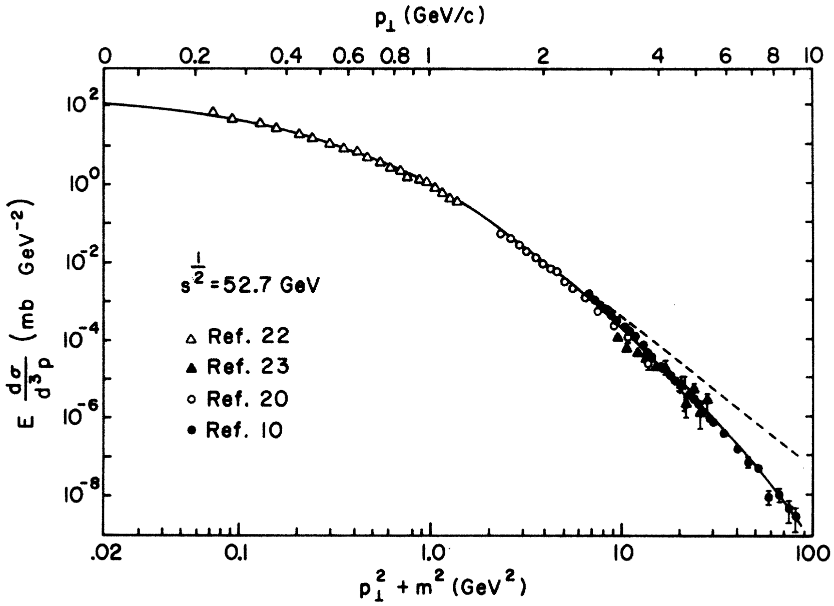

FIG. 6. The single-particle spectrum at $x_\parallel = 0$ for $pp \to \pi + X$ for large and small transverse momentum. The solid line is our result from Sec. III for $s^{1/2} = 52.7$ GeV and $a^2 = 0.39$ GeV^2; the dashed line is for $s \to \infty$. The normalization of the data of different groups appears slightly different, and we have moved the data of Refs. 21 and 22 up by a factor of 1.3.

Neglecting the second term on the left-hand side, we obtain for the turnover point

$$x_\perp \approx 1.1/s^{1/3} . \qquad (3.11)$$

We can also compare to data[20] away from 90° such as those shown in Fig. 5 which are at $\theta_{c.m.} = 60°$. In Fig. 7 our predictions for other angles are shown for $r \equiv (x_\perp{}^2 + x_\parallel{}^2)^{1/2} = 0.1$, 0.5, and 0.9. This angular dependence might be a good means of differentiating between different models. The predictions of the BBS model,[7] for example, rise considerably above those of this model as $z = \cos\theta_{c.m.}$ increases, especially for large r.

C. Variation with energy of the height of the central plateau from double-Pomeron exchange

Small transverse momenta determine the height of the central plateau $d\sigma/dy$ or the coefficient of $\ln s$ in $\langle n \rangle$. With the assumption that the absorptive amplitudes A_l and A_r are Pomeron-dominated, our results indicate a rise of $d\sigma/dy(y=0)$ with energy over the range of energies at the CERN ISR which is in agreement with experimental findings. At lower energies ($E_{lab} \approx 20$ GeV), our calculations of double-Pomeron exchange fall below the data. The rise of the calculated double-Pomeron contribution by a factor of 2.3 from $s = 47$ to 2800 GeV^2 must be taken into account before the non-Pomeron contributions can be discussed. These results are similar to those obtained by Caneschi,[16] but now include power-law damping and Bjorken-scaling functions.

D. Secondary trajectories

The Pomeron is present through the factor ω in $A \propto \omega\chi(\omega)$. The effect of secondary trajectories will appear in the form $\omega^{1/2}\chi'(\omega)$ since the Bjorken-scaling behavior is independent of the Regge intercept.[13,14] To examine only the effect of secondaries we took $\chi' = \chi$ and computed with $(\omega + \omega^{1/2}) \times \chi(\omega)$.

To obtain a similar fit to that in Fig. 6 it was necessary to change a^2 only from 0.39 to 0.34 GeV^2. Since only the dependence on ω was changed, the energy dependence, including secondary trajectories, is still s^{-4} in the fixed-$x_\perp$ scaling region.

E. K/π and K^+/K^- production ratios

As $x_\perp$ increases away from zero, the dominant contribution comes from the region where s_l' and s_r' are near threshold. As a result the thresholds s_1 and s_3 and dynamical behavior in the threshold region become very important.

Their role is particularly evident in the produced particle ratios. For $pp \to \pi X$, $s_1 = s_3 = (m_p + m_\pi)^2$, but for $pp \to K^+X$, s_1(or s_3) $= (m_\Lambda + m_\pi)^2$, and for $pp \to K^-X$, s_1(or s_3) $= (m_p + m_K)^2$. In a pre-

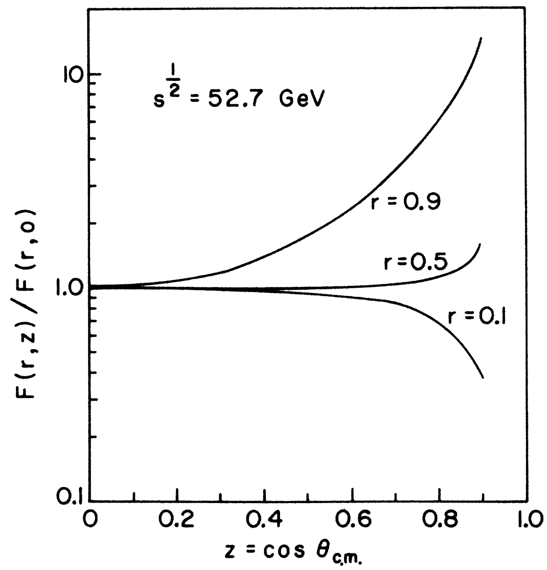

FIG. 7. The angular dependence of the scaling function $F(r,z) = p_\perp{}^8 E\, d\sigma/d^3p$ for $pp \to \pi + X$ predicted in Sec. III for $s^{1/2} = 52.7$ GeV.

vious work[17] we examined the K/π ratio at $s \to \infty$ with $\chi(\omega) = (\omega - 1)/\omega$. The results obtained here for K^+/π^+ are very similar, but are now in complete agreement with the data at large $p_\perp$ and a little closer to the data at small $p_\perp$.

Since the K^- threshold is higher than the K^+ threshold, the K^-/K^+ ratio will be less than one and decreases as $x_\perp$ increases. The lack of resonances in the exotic channel K^+p relative to K^-p would be reflected in $A(s_l', t_l)$ and further contribute to the shrinking K^-/K^+ ratio.

ACKNOWLEDGMENTS

We would like to thank M. Bander and R. Blankenbecler for helpful discussions. We also wish to acknowledge the hospitality of the Aspen Center for Physics and the Stanford Linear Accelerator Center.

APPENDIX A: RELATION OF GENERAL PERIPHERAL APPROACH TO PARTON APPROACH

The general peripheral approach of Sec. III can be related to the results of Sec. II by performing the t_l, t_r, and s_r' integrations and converting the s_l' integral to an x_1 integration. This is the procedure followed by ACT[3] in proving scaling, but here we generalize to include absorptive parts which are not solutions to a multiperipheral integral equation. For t_l, s_l' becoming $O(s)$ and s_r', t_r damped independent of s, we have for the effective incoming parton distribution

$$(gm)^2 P(x_1) = (-t_l) A(s_l', t_l)\,, \tag{A1}$$

where

$$x_1 = \left(\frac{s_l'}{-t_l} + 1\right)^{-1}\,. \tag{A2}$$

Also in this region, we find the t_l integration limits from Eq. (B4) using $u_l \cong -sx_-$, $u_r \cong -sx_+$, and $M^2 \cong s(1 - x_+ - x_-)$:

$$t_{3,4} = -x_+ \frac{s_l' + sx_-}{1 - x_+} \pm O(\sqrt{s})\,. \tag{A3}$$

The absorptive parts have $t_l \equiv t$ approximately fixed at this value of $O(s)$, and the integration becomes approximately

$$\int_{t_3}^{t_4} dt_l \frac{1}{(-\Delta_4)^{1/2}} = \frac{1}{s(1-x_+)} \int_{t_3}^{t_4} dt_l [(t_4 - t_l)(t_l - t_3)]^{-1/2} = \frac{\pi}{s(1-x_+)}\,. \tag{A4}$$

With this approximation of neglecting external masses we have from Eq. (3.6) in this region $[s_r \equiv (p + p_r)^2]$

$$E\frac{d\sigma}{d^3p} = \frac{\pi (gm)^4}{s^2(1-x_+)} \times \int_0^{M^2} \frac{ds_l'}{-t} \left[\int_{-\infty}^{0} \frac{dt_r}{(a^2 - t_r)^2} \times \int_0^{t_r s_r/t} ds_r' A(s_r', t_r) \right] \frac{1}{t^2} P(x_1)\,. \tag{A5}$$

Changing variables to

$$x_2' = \left(\frac{s_r'}{-t_r} + 1\right)^{-1}, \quad x_2 \equiv \left(\frac{s_r}{-t} + 1\right)^{-1}, \tag{A6}$$

assuming scaling

$$(-t_r) A(s_r', t_r) = P(x_2')(gm)^2\,, \tag{A7}$$

and then performing the t_r integration gives for the bracketed quantity in (A5)

$$\frac{\tilde{P}(x_2)}{x_2} \equiv \frac{1}{a^2} \int_{x_2}^{1} dx_2' \frac{P(x_2')}{x_2'^2}\,. \tag{A8}$$

The kinematics gives

$$\frac{x_+}{x_1} + \frac{x_-}{x_2} = 1, \quad t = -sx_1 x_-\,. \tag{A9}$$

Introducing $y = x_+/x_1$ and $P(x_1) = F(x_1)/x_1$, $\tilde{P}(x_2) = \tilde{F}(x_2)/x_2$, we have as in Eq. (2.14)

$$E\frac{d\sigma}{d^3p} = \frac{\pi g^6 m^6}{a^2 p_\perp{}^8} \int_{x_+}^{1-x_-} dy\, F\left(\frac{x_+}{y}\right) \tilde{F}\left(\frac{x_-}{1-y}\right) (1-y)^3 y\,. \tag{A10}$$

In Sec. III we have used the scaling functions to fit the data:

$$P(x_1)=\frac{(1-x_1)^3}{x_1}\ ,\quad P(x_2')=\frac{(1-x_2')^3}{x_2'}\ . \tag{A11}$$

Putting $P(x_2')$ in Eq. (A8) gives the result

$$\bar{P}(x_2)=\frac{1}{2x_2}\left[(1-x_2)(1-5x_2-2x_2{}^2)+6x_2{}^2\ln(1/x_2)\right]. \tag{A12}$$

The calculation of the cross section by Eq. (A10) using the above forms (A11) and (A12) for $P(x_1)$ and $\bar{P}(x_2)$ agrees to within 20% with the exact calculation in Sec. III using the precursor $P(x_2')$ from Eq. (A11). This justifies the approximations in Eq. (A3) and the neglect of masses used in deriving scaling. Also, the geometric mean of $P(x_1)$ and $\bar{P}(x_2)$ is close to $P(x)=(1-x)^4/x$ as found in Sec. II to fit the ISR data.

APPENDIX B: DEFINITIONS FOR QUANTITIES IN EQ. (3.6)

The limits of integration except the thresholds s_1 and s_3 (which are discussed in Sec. III E) are found by solving $\Delta_4 \leq 0$ [from $\theta(-\Delta_4)$ in Eq. (3.6)]. The results are

$$s_1=(m_2+m_\pi)^2\ ,\quad s_3=(m_1+m_\pi)^2\ , \tag{B1}$$

$$s_2=(M-s_3{}^{1/2})^2\ ,\quad s_4=(M-s_r'{}^{1/2})^2\ , \tag{B2}$$

$$t_{1,2}=\frac{1}{2M^2}\left[f_2f_3-2M^2f_1\mp\Delta_1{}^{1/2}\Delta^{1/2}(M^2,s_l',s_r')\right]\ , \tag{B3}$$

$$t_{3,4}=(F_1\mp F_2)/\Delta_1\ , \tag{B4}$$

$$\Delta_4=\begin{vmatrix} 2s_l' & f_2 & s_l'-t_l+m_1{}^2 & f_1+t_r \\ f_2 & 2M^2 & f_4 & f_3 \\ s_l'-t_l+m_1{}^2 & f_4 & 2m_1{}^2 & f_5 \\ f_1+t_r & f_3 & f_5 & 2m_2{}^2 \end{vmatrix}\ , \tag{B5}$$

where (note that f_3, f_4, and f_5 are not functions of the variables of integration)

$$\begin{aligned} &f_1=(M^2-u_l-s_r'),\quad f_4=(M^2-u_r+m_1{}^2)\ ,\\ &f_2=(M^2+s_l'-s_r'),\quad f_5=(s-m_1{}^2-m_2{}^2)\ ,\\ &f_3=(M^2-u_l+m_2{}^2),\quad \Delta_1=\Delta(M^2,u_l,m_2{}^2)\ , \end{aligned} \tag{B6}$$

with

$$\Delta(a,b,c)\equiv a^2+b^2+c^2-2ab-2ac-2bc\ .$$

For the definition of t_3 and t_4 we have

$$F_1=(s_l'+m_1{}^2)\Delta_1-t_r(f_3f_4-2M^2f_5)-f_1f_3f_4+2M^2f_1f_5-f_2f_3f_5+2m_2{}^2f_2f_4\ , \tag{B7}$$

$$\begin{aligned} F_2=2&[-M^2\Delta(s,m_1{}^2,m_2{}^2)-m_2{}^2f_4{}^2-m_1{}^2f_3{}^2+f_3f_4f_5]^{1/2}\\ &\times[-M^2t_r{}^2+t_r(f_2f_3-2M^2f_1)-M^2f_1{}^2-m_2{}^2f_2{}^2-s_l'\Delta_1+f_1f_2f_3]^{1/2}\ . \end{aligned} \tag{B8}$$

For the following, see Fig. 1:

$$\begin{aligned} M^2&=(p_a+p_b-p)^2\\ &=(p_l+p_r)^2\\ &=s+u_l+u_r-m_1{}^2-m_2{}^2-\mu^2\ , \end{aligned} \tag{B9}$$

$$\begin{aligned} u_l&=(p_a-p)^2\\ &=m_1{}^2+\mu^2-(s+m_1{}^2-m_2{}^2)E/s^{1/2}+p_\parallel\Delta^{1/2}(s,m_1{}^2,m_2{}^2)/s^{1/2}\ , \end{aligned} \tag{B10}$$

$$\begin{aligned} u_r&=(p_b-p)^2\\ &=m_2{}^2+\mu^2-(s-m_1{}^2+m_2{}^2)E/s^{1/2}-p_\parallel\Delta^{1/2}(s,m_1{}^2,m_2{}^2)/s^{1/2}\ . \end{aligned} \tag{B11}$$

μ, E, and $p_\parallel$ are the mass, energy, and parallel momentum of the produced particle in the center-of-mass system. m_1, m_2 are the masses of the left and right incoming particles.

---

*Work supported in part by the National Science Foundation.

[1] W. R. Frazer *et al.*, Rev. Mod. Phys. 44, 284 (1972), and references therein.

[2] M. Barnett and D. Silverman, Phys. Lett. 44B, 28 (1973); Phys. Rev. D 8, 2108 (1973).

[3] D. Amati, L. Caneschi, and M. Testa, Phys. Lett. 43B, 186 (1973); CERN Report No. TH-1644 (unpublished).

[4] D. Amati, S. Fubini, and A. Stanghellini, Nuovo Cimento 26, 896 (1962); L. Bertocchi, S. Fubini, and M. Tonin, *ibid.* 25, 626 (1962).

[5] S. M. Berman, J. D. Bjorken, and J. B. Kogut, Phys. Rev. D 4, 3388 (1971).

[6] R. Blankenbecler, S. J. Brodsky, and J. F. Gunion, Phys. Lett. 42B, 461 (1972); Phys. Rev. D 6, 2652 (1972).

[7] M. Bander, M. Barnett, and D. Silverman, Phys. Lett. 48B, 243 (1974).

[8] P. V. Landshoff and J. C. Polkinghorne, Phys. Rev. D 8, 4157 (1973).

[9] P. V. Landshoff and J. C. Polkinghorne, Phys. Rev. D 8, 927 (1973); Phys. Lett. 45B, 361 (1973); Phys. Rep. 5C, 1 (1972).

[10] F. W. Büsser *et al.*, Phys. Lett. 46B, 471 (1973).

[11] D. Silverman, in preparation.

[12] J. Cronin *et al.*, Phys. Rev. Lett. 31, 1426 (1973).

[13] G. Tiktopoulos and S. B. Treiman, Phys. Rev. 135, B7711 (1964); 136, B1217 (1964).

[14] H. D. I. Abarbanel, M. L. Goldberger, and S. B. Treiman, Phys. Rev. Lett. 22, 500 (1969).

[15]J. Kogut and L. Susskind, Phys. Rep. 8C, 75 (1973), and references contained therein.

[16]L. Caneschi, Nucl. Phys. B68, 77 (1974).

[17]R M. Barnett, D. Silverman, M. D. Scadron, and R. L. Thews, Phys. Rev. D 9, 2195 (1974). With the approach used in this reference, and with the addition of $\chi(\omega) = (\omega - 1)^3/\omega^3$, one fits the data with $a^2 = 0.58$ GeV^2.

[18]S. D. Ellis and M. B. Kislinger, Phys. Rev. D 9, 2027 (1974).

[19]D. Silverman and C.-I Tan, Nuovo Cimento 2A, 489 (1971).

[20]B. Alper *et al.*, Phys. Lett. 44B, 521 (1973); 44B, 527 (1973); see also 47B, 75 (1973); and 47B, 275 (1973).

[21]M. Banner *et al.*, Phys. Lett. 41B, 547 (1972).

[22]M. Banner *et al.*, Phys. Lett. 44B, 537 (1973).

[23]D. Silverman and P. Ting, Nucl. Phys. B35, 445 (1971).